Constraint of non-methane volatile organic compound emissions with TROPOMI HCHO observations and its impact on summertime surface ozone simulation over China

Shuzhuang Feng[1], Fei Jiang[1,2,5*], Tianlu Qian[3], Nan Wang[4], Mengwei Jia[1], Songci Zheng[1], Jiansong Chen[6], Fang Ying[6], Weimin Ju[1,2]

[1] *Jiangsu Provincial Key Laboratory of Geographic Information Science and Technology, International Institute for Earth System Science, Nanjing University, Nanjing, 210023, China*

[2] *Jiangsu Center for Collaborative Innovation in Geographical Information Resource Development and Application, Nanjing, 210023, China*

[3] *School of Geographic and Biologic Information, Nanjing University of Postsand Telecommunications, Nanjing, 210023, China*

[4] *College of Carbon Neutrality Future Technology, Sichuan University, Chengdu, 610207, China*

[5] *Frontiers Science Center for Critical Earth Material Cycling, Nanjing University, Nanjing, 210023, China*

[6] *Hangzhou Municipal Ecology and Environment Bureau, Hangzhou, 310020, China*

* Corresponding author: Tel.: +86-25-83597077; Fax: +86-25-83592288; E-mail address: jiangf@nju.edu.cn

Abstract

Non-methane volatile organic compounds (NMVOC), serving as crucial precursors of O_3, have a significant impact on atmospheric oxidative capacity and O_3 formation. However, both anthropogenic and biogenic NMVOC emissions remain subject to considerable uncertainty. Here, we extended the Regional multi-Air Pollutant Assimilation System (RAPAS) with the EnKF algorithm to optimize NMVOC emissions in China by assimilating TROPOMI HCHO retrievals. We also simultaneously optimize NO_x emissions by assimilating in-situ NO_2 observations to address the chemical feedback among VOC-NO_x-O_3. Furthermore, a process-based analysis was employed to quantify the impact of NMVOC emission changes on various chemical reactions related to O_3 formation and depletion. NMVOC emissions exhibited a substantial reduction of 50.2%, especially in forest-rich areas of central and southern China, revealing a prior overestimation of biogenic NMVOC emissions. The RAPAS significantly improved HCHO simulations, reducing biases by 75.7%, indicating a notable decrease in posterior emission uncertainties. Moreover, the posterior NMVOC emissions significantly corrected the prior overestimation in O_3 simulations, reducing biases by 49.3%. This can be primarily attributed to a significant decrease in the $RO_2 + NO$ reaction rate and an increase in the $NO_2 + OH$ reaction rate in the afternoon, thus limiting O_3 generation. Sensitivity analyses emphasized the necessity of considering both NMVOC and NO_x emissions for a comprehensive assessment of O_3 chemistry. This study enhances our understanding of the effects of NMVOC emissions on O_3 production and can contribute to the development of effective emission reduction policies.

1 Introduction

Since the Chinese government implemented the Air Pollution Prevention and Control Action Plan in 2013, there has been a notable reduction in NO_x emissions (Zheng et al., 2018). However, despite these advancements, the issue of O_3 pollution persists and, in certain cases, has shown signs of worsening (Ren et al., 2022). The increase in O_3 concentration can be attributed not only to adverse meteorological conditions but also predominantly to unbalanced joint control of non-methane volatile organic compounds (NMVOCs) and nitrogen oxides (NO_x) (Li et al., 2020). NMVOCs are vital precursors of O_3 and have a substantial impact on the atmospheric oxidation capacity, thereby altering the lifetimes of other pollutants. Accurately quantifying NMVOC emissions holds significant importance in investigating their impact on O_3 chemistry and in formulating emission reduction policies.

Anthropogenic NMVOC emissions have traditionally been estimated using a "bottom-up" method. However, the accuracy and timeliness of these estimations face challenges owing to the scarcity of local measurements for emission factors, the incompleteness and unreliability of activity data, and the diverse range of species and technologies involved (Cao et al., 2018; Hong et al., 2017). Furthermore, uncertainties arise in model-ready NMVOC emissions due to spatial and temporal allocations using various "proxy" data for different source sectors (Li et al., 2017a). Li et al. (2021) reported substantial discrepancies among emission estimates in various studies, ranging 23% to 56%. Biogenic NMVOC emissions are typically estimated using models like the Model of Emissions of Gases and Aerosols from Nature (MEGAN) (Guenther et al., 2012) and the Biogenic Emission Inventory System (BEIS) (Pierce et al., 1998). NMVOC emissions result from the multiplication of plant-specific standard emission rates by dimensionless activity factors. Nonetheless, apart from inaccuracies in the distribution of plant functional types, empirical parameterization, especially concerning responses to temperature and drought stress, can introduce substantial uncertainties (Angot et al., 2020; Seco et al., 2022; Jiang et al., 2018). Warneke et al. (2010) determined isoprene emission rates through field measurements and conducted a comparison with MEGAN and BEIS estimates, revealing a notable tendency for MEGAN to overestimate emissions, while BEIS consistently underestimated them. Similarly, Marais et al. (2014) found that MEGAN's isoprene emission estimates were 5-8 times higher than the canopy-scale flux measurements obtained from African field campaigns.

A top-down approach, utilizing observed data, has been developed for estimating VOCs emissions. For instance, based on aircraft and ground-based field measurements, the source-receptor relationships algorithm with Lagrangian particle dispersion model (Fang et al., 2016), mixed layer gradient techniques (Mo et al., 2020), eddy covariance flux measurements (Yuan et al., 2015), and box model (Wang et al., 2020) have been employed to complement or verify bottom-up results. However, these approaches do not comprehensively consider the complex nonlinear chemical reactions and transport processes that VOCs undergo in the atmosphere. Formaldehyde (HCHO) and glyoxal (CHOCHO) in the atmosphere serve as crucial oxidization intermediates for various VOCs (Hong et al., 2021; Liu et al., 2012). Satellite-based observations can readily detect their presence in the form of vertical column density (VCD) from space, making them widely utilized for estimating NMVOC emissions. A commonly used approach assumes that the observed HCHO/CHOCHO columns are locally linearly correlated with VOC emission rates (Palmer et al., 2006; Liu et al., 2012). However, this approach does not consider the spatial offset resulting from chemistry reactions and transport processes. Chaliyakunnel et al. (2019) conducted a Bayesian analysis to derive an optimal estimate of VOC emissions using HCHO measurements over the Indian subcontinent. Their results indicated that biogenic VOC emissions modeled by MEGANv2.1 were overestimated by approximately 30–60%, whereas anthropogenic VOC emissions derived from the RETRO inventory were underestimated by 13–16%. Cao et al. (2018) employed the GEOS-Chem model and its adjoint, incorporating tropospheric HCHO and CHOCHO column data from the GOME-2A and OMI satellites as constraints, to quantify Chinese NMVOC emissions. They demonstrated a low bias in the MEGAN model, in contrast to the significant overestimation shown in Bauwens et al. (2016), especially in southern China.

Several investigations have been conducted to explore the implications of inverted VOC emissions on surface O_3. For instance, using the Eulerian box model, Zhou et al. (2023) employed concurrent VOC measurements to constrain anthropogenic VOC emissions. This led to improved simulations of VOCs and O_3, with a reduction in high emissions by 15%–36% in the Pearl River Delta (PRD) region. Local model biases in simulating the oxidation of NMVOCs and O_3 are closed related to uncertainties in NO_x emissions (Wolfe et al., 2016; Chan Miller et al., 2017). To tackle these critical questions, Kaiser et al. (2018) applied an adjoint algorithm to estimate isoprene

124 emission over the southeast US by downwardly adjusting anthropogenic NO_x emissions

125 by 50% to rectify NO_2 simulations. Their findings indicated that isoprene emissions

126 from MEGAN v2.1 were overestimated by an average of 40%, slightly lower than the

127 50% reduction in Bauwens et al. (2016). Souri et al. (2020) simultaneously optimized

128 NMVOC and NO_x emissions utilizing OMPS-NM HCHO and OMI NO_2 retrievals in

129 East Asia. They found that predominantly anthropogenic NMVOC emissions from

130 MIX-Asia 2010 increased over the North China Plain (NCP), whereas predominantly

131 biogenic NMVOC emissions from MEGAN v2.1 decreased over southern China after

132 the adjustment. Unfortunately, the posterior simulations exacerbated the overestimation

133 of O_3 levels in northern China.

134 Most studies regarding the inversion of NMVOC emissions or its impact on O_3

135 neglected the uncertainties associated with NO_x-dependent production or loss of

136 NMVOC oxidation and O_3. An iteratively nonlinear joint inversion of NO_x and

137 NMVOCs using multi-species observations is expected to minimize the uncertainties

138 in their emissions and is well-suited to address the intricate relationship among VOC-

139 NO_x-O_3. In this study, we extended the Regional multi-Air Pollutant Assimilation

140 System (RAPAS) upon the ensemble Kalman filter (EnKF) assimilation algorithm to

141 enhance the optimization of NMVOC emissions over China, utilizing the

142 TROPOspheric Monitoring Instrument (TROPOMI) HCHO retrievals with high spatial

143 coverage and resolution. To more accurately quantify the impact of NMVOC emissions

144 on O_3, NO_x emissions were simultaneously adjusted using nationwide in-situ NO_2

145 observations. Process analysis was subsequently employed to quantify various

146 chemical pathways associated with O_3 formation and loss. Through a top-down

147 constraint on both emissions, this study aims to offer a more scientific insight into the

148 consequences of optimizing NMVOC emissions on O_3 and contribute to the

149 development of appropriate emission reduction policies.

150 **2 Data and Methods**

151 **2.1 Data Assimilation System**

152 The RAPAS system (Feng et al., 2023) has been developed based on a regional

153 chemical transport model (CTM) and ensemble square root filter (EnSRF) assimilation

154 modules (Whitaker and Hamill, 2002), which are employed for simulating atmospheric

155 compositions and inferring anthropogenic emissions by assimilating surface

156 observations, respectively (Feng et al., 2022; Feng et al., 2020). The inversion process

157 follows a two-step procedure within each inversion window. The two-step inversion

158 strategy facilitates error propagation and iterative emission optimization, which have

159 proven the superiority and robustness of our system in estimating emissions (Feng et

160 al., 2023). In this study, we extended the data frame to include the assimilation of

161 TROPOMI HCHO retrievals for optimizing NMVOC emissions. Concise descriptions

162 of the forecast model, data assimilation approach, and experimental settings follow.

2.1.1 Atmospheric Transport Model

164 The Weather Research and Forecast (WRF v4.0) model (Skamarock and Klemp, 2008)

165 and the Community Multiscale Air Quality Modeling System (CMAQ v5.0.2) (Byun

166 and Schere, 2006) were applied to simulate meteorological conditions and atmospheric

167 chemistry, respectively. WRF simulations were conducted with a 27-km horizontal

168 resolution, covering the entire mainland China on a grid of 225×165 cells (Figure 1).

169 The CMAQ model was run over the same domain, but with a removal of three grid cells

170 on each side of the WRF domain. The vertical settings in WRF and CMAQ was the

171 same as Feng et al. (2020). To account for the rapid expansion of urbanization, we

172 updated underlying surface information for urban and built-up land using the MODIS

173 Land Cover Type Product (MCD12C1) Version 6.1 of 2022. Chemical lateral boundary

174 conditions were extracted from the output of the global CTM Whole Atmosphere

175 Community Climate Model (WACCM) with a resolution of $0.9° \times 1.25°$ at 6-hour

176 intervals (Marsh et al., 2013). In the first data assimilation (DA) window, chemical

177 initial conditions also originated from WACCM output, whereas in subsequent

178 windows, they were derived through forward simulation using optimized emissions

179 from the previous window. Table S1 lists the detailed physical and chemical

180 configurations. To assess the impact of updated NMVOC emissions on O_3 production

181 efficiency, we further decoupled the contribution of the primary chemical processes to

182 the O_3 levels using the CMAQ Integrated Reaction Rate (IRR) analysis.

2.1.2 EnKF Assimilation Algorithm

184 The emissions are constrained using the Ensemble Square Root Filter (EnSRF)

185 algorithm introduced by Whitaker and Hamill (2002). This approach fully accounts for

186 temporal and geographical variations in both the transportation and chemical reactions

187 within the emission estimates. During the forecast step, the background ensembles are

188 derived by applying perturbation to the prior emissions. The perturbed samples are
189 typically drawn from Gaussian distributions with a mean of zero and a standard
190 deviation equal to the prior emission uncertainty in each grid cell. Ensemble runs of the
191 CMAQ model were subsequently performed to propagate the background errors with
192 each ensemble sample of state vectors.

193 In the analysis step, the ensemble mean $\overline{X^a}$ of the analyzed state is regarded as the best
194 estimate of emissions, which is obtained by updating the background ensemble mean
195 through the following equations:

$$\overline{X^a} = \overline{X^b} + \mathbf{K}(\mathbf{y} - H\overline{X^b}) \tag{1}$$

$$\mathbf{K} = P^b H^T (H P^b H^T + R)^{-1} \tag{2}$$

198 where $\mathbf{y}$ is the observational vector; H represents the observation operator mapping
199 model space to observation space; The expression $\mathbf{y} - H\overline{X^b}$ quantifies the disparities
200 between simulated and observed concentrations; $P^b H^T$ illustrates how uncertainties in
201 emissions relate to uncertainties in simulated concentrations; The Kalman gain matrix
202 $\mathbf{K}$, dependent on background error covariance P^b and observation error covariance R,
203 determines the relative contributions to the updated analysis.

204 State variables for emissions include NO_x and NMVOCs. To reduce the degree of
205 freedom in the analysis and avoid the difficulty associated with estimating spatio-
206 temporal variations in background errors for individual species, we focus on optimizing
207 the lumped total NMVOC emissions. During the forecast step, we differentiate
208 individual NMVOC species emissions from the total NMVOC emissions using bottom-
209 up statistical information. For a consistent comparison between simulations and
210 observations, model-simulated NO_2 were diagnosed at the time and location of surface
211 NO_2 measurements, whereas model-simulated HCHO was horizontally sampled to
212 align with TROPOMI HCHO VCD retrievals, and subsequently integrated vertically.

213 In this study, the DA window was set to one day and daily TROPOMI HCHO columns
214 were utilized as observational constraints in our inversion framework. The ensemble
215 size was set to 50 to strike a balance between computational cost and inversion accuracy.
216 To reduce the impact of unrealistic long-distance error correlations, the Gaspari and
217 Cohn function (Gaspari and Cohn, 1999) was utilized as covariance localization to
218 ensure the meaningful influence of observations on state variables within a specified

219 cutoff radius, while mitigating their negative impacts on distant state variables. The

220 optimal localization scale is interconnected with factors such as the assimilation

221 window, the dynamic system, and the lifetime of chemical species. Given the average

222 wind speed of 2.8 m/s (Table S2) and a DA window of 1 day, the localization scales for

223 NO_2 and HCHO, both characterized as highly reactive species with lifespans of just a

224 few hours, were set to 150 km and 100 km, respectively.

2.2 Observation Data and Errors

226 Considering the availability of HCHO data, we utilized daily offline retrievals of

227 tropospheric HCHO columns from Sentinel-5P (S5P) L3 TROPOMI data obtained

228 through Google Earth Engine (De Smedt et al., 2018). The S5P satellite follows a near-

229 polar sun-synchronous orbit at an altitude of 824 km with a 17-day repeating cycle. It

230 crosses the Equator at 13:30 local solar time (LST) on the ascending node. The spatial

231 resolution at nadir was refined to $3.5 \times 5.5 \, km^2$ on 6 August 2019. Following the

232 recommendations in the S5P HCHO product user manual, we filtered the source data

233 to exclude pixels with qa_value less than 0.5 for HCHO column number density and

234 0.8 for aerosol index (AER_AI). The remaining high-quality pixels with minimal

235 snow/ice or cloud interference are averaged to 27-km grids. Figure 1b illustrates the

236 coverage and data amount of TROPOMI HCHO retrievals in August 2022 after

237 processing. Although the distribution of filtered data exhibits spatial non-uniformity,

238 most grid cells have observational coverage for over half of the time, particularly in the

239 southern region of China where NMVOC emissions are higher. We assigned

240 measurement errors of 30% to TROPOMI HCHO columns based on validation against

241 a global network of 25 ground-based Fourier transform infrared (FTIR) column

242 measurements (Vigouroux et al., 2020). The representation error can be disregarded

243 because the model's resolution significantly surpasses that of the TROPOMI pixels.

244 To address the chemical feedback among VOC-NO_x-O_3, we also simultaneously

245 optimized NO_x emissions by assimilating in-situ NO_2 observations. The extensively

246 covered and high-precision monitoring network can provide sufficient constraints for

247 emission inversion (Figure 1a). Hourly averaged surface NO_2 observations from

248 national control air quality stations obtained from the Ministry of Ecology and

249 Environment of the People's Republic of China (http://106.37.208.228:8082/, last

250 access: 5 May 2023). In case where multiple stations are located within the same grid,

251 a random site is chosen for validation, while the remaining sites are averaged to mitigate

252   the impact of error correlation (Houtekamer and Zhang, 2016) for assimilation. In total,

253   1276 stations were chosen for assimilation and an additional 425 independent stations

254   were selected for verification (Figure 1a). The observation error covariance matrix $\boldsymbol{R}$

255   incorporates contributions from both measurement and representation errors. The

256   measurement error is defined as $\varepsilon_0 = 1.0 + 0.005 \times \Pi_0$, where Π_0 represents the

257   observed NO_2 concentration. Following the approach of Elbern et al. (2007) and Feng

258   et al. (2018), the representative error is defined as $\varepsilon_r = \gamma \varepsilon_0 \sqrt{\Delta l / L}$, where γ is a tunable

259   parameter (here, γ=0.5), Δl is the grid spacing (27 km), and L is the radius (here, L=0.5)

260   of the observation's influence area. The total observation error (r) was defined as $r =$

261    $\sqrt{\varepsilon_0^2 + \varepsilon_r^2}$. The observation errors are assumed to be uncorrelated so that $\boldsymbol{R}$ is a

262   diagonal matrix.

263

264
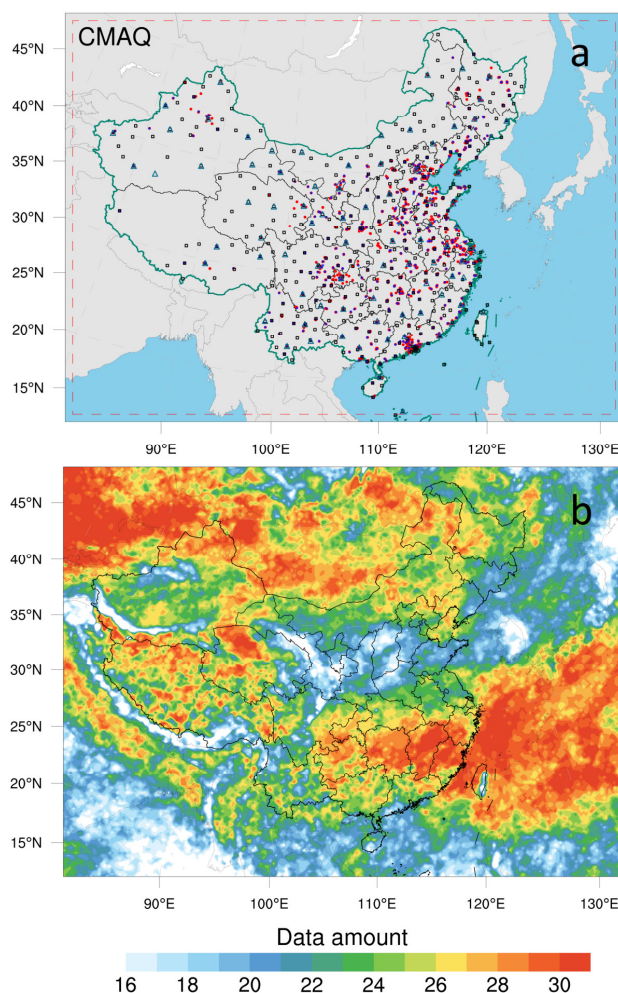
Figure 1. Model domain and observation network (a) and data amount of TROPOMI
HCHO retrievals during August 2022 in each grid (b). The red dashed frame delineates
the CMAQ computational domain; black squares denote surface meteorological
measurement sites; navy triangles indicate sounding sites (Text S1), and red and blue
dots represent air pollution measurement sites.

2.3 Prior Emissions and Uncertainties

The prior anthropogenic NO_x and NMVOC emissions for China were obtained from
the most recent Multi-resolution Emission Inventory for China of 2020 (MEIC,
http://www.meicmodel.org/, last access: 8 May 2023) (Zhang et al., 2009). For
anthropogenic emissions outside China, we utilized the mosaic Asian anthropogenic
emission inventory (MIX) for the base year of 2010 (Li et al., 2017b). The daily

10

276 emission inventory, which was arithmetically averaged from the combined monthly

277 emission inventory, was employed as the first guess. Ship emissions were derived from

278 the shipping emission inventory model (SEIM) for 2017, which was calculated based

279 on the observed vessel automatic identification system (Liu et al., 2017). Biomass

280 burning emissions were retrieved from the Global Fire Emissions Database version 4.1

281 (GFEDv4, https://www.globalfiredata.org/, last access: 8 May 2023) (van der Werf et

282 al., 2017; Mu et al., 2011). Biogenic NO_x and NMVOC emissions were calculated using

283 the Model of Emissions of Gases and Aerosols from Nature (MEGAN) developed by

284 Guenther et al. (2012).

285 As previously mentioned, the optimized emissions are transferred to the next DA

286 window as prior emissions for iterative inversion. For biogenic emissions, it is

287 decomposed into hourly scales based on the daily varying temporal profiles in MEGAN

288 as model inputs. Daily emission variations will largely dominate the uncertainty in

289 emissions. Taking into account compensating for model errors and avoiding filter

290 divergence, we consistently applied an uncertainty of 25% to each model grid of NO_x

291 emissions at each DA window, as in Feng et al. (2020). NMVOC emissions typically

292 exhibit greater uncertainties compared to NO_x emissions (Li et al., 2017b). Based on

293 model evaluation, the uncertainty of NMVOC emissions was set to 40% (Kaiser et al.,

294 2018; Souri et al., 2020; Cao et al., 2018). This study also addresses uncertainties in

295 emissions for CO, SO_2, primary $PM_{2.5}$, and coarse PM_{10} to consider the chemical

296 feedback between different species following Feng et al. (2023).

3 Experimental Design

298 Before implementing the emission inversion, a relatively perfect initial field is

299 generated at 0000 UTC on August 01 through conducting a 5-day simulation with 6-

300 hour interval 3D-Var data assimilation. Subsequently, daily emissions are continuously

301 updated over the entire month of August (EMDA). To validate the posterior emissions

302 of NO_x and NMVOCs, we compared two parallel forward simulation experiment with

303 NO_2 and HCHO measurements, denoted as CEP and VEP, corresponding to prior and

304 posterior emission scenarios, respectively. To investigate the impact of optimizing

305 NMVOC emissions on the secondary production and loss of surface O_3, a forward

306 simulation experiment (CEP1) was conducted with the prior NMVOC emissions and

307 the posterior NO_x emissions. Additionally, we designed three sensitivity experiments to

308 investigate the robustness of the constrained NMVOC emissions. EMS1 involved

11

309   doubling the background error from 40% to 80% to investigate the influence of

310   background error settings. EMS2 aimed to evaluate the effect of observational data

311   retrieval errors on emission estimates, in which HCHO columns were empirically bias-

312   corrected based on error characteristics (Souri et al., 2021). EMS3 aimed to illustrate

313   the significance of optimizing NO_x emission in quantifying VOC-O_3 chemical reactions.

314   In this experiment, NO_x emissions were not optimized. Two forward modelling

315   experiments (CEP2 and CEP3) were also performed using the posterior emissions of

316   EMS2 and EMS3 to evaluate their performance. All experiments employ identical

317   meteorological fields, as well as the same gas-phase and aerosol modules. Table 1

318   summarizes the different emission inversion and validation experiments conducted in

319   this study.

320   **Table 1**. The assimilation, sensitivity, and validation experiments conducted in this

321   study.

Exp.Type	Exp. Name	NMVOC emissions	NO_x emissions	Assimilated HCHO retrievals
Assimilation	EMDA	MEIC 2020 and MEGAN for August (the first DA window), optimized emissions of the previous window (other DA windows)	MEIC 2020 and MEGAN for August (the first DA window), optimized emissions of the previous window (other DA windows)	Default
Sensitivity	EMS1	Same as EMDA but with doubled default uncertainty	Same as EMDA	Default
	EMS2	Same as EMDA	Same as EMDA	Reduce by 25% in regions with observations $< 2.5 \times 10^{15}$ molec cm^{-2} and increase by 30% in regions with observations $> 8 \times 10^{15}$ molec cm^{-2}
	EMS3	Same as EMDA	MEIC 2020 and MEGAN for August	Default
Validation	CEP	MEIC 2020 and MEGAN for August	MEIC 2020 and MEGAN for August	\
	VEP	Posterior emissions of EMDA	Posterior emissions of EMDA	\
	CEP1	Same as CEP	Posterior emissions of EMDA	\
	CEP2	Posterior emissions of EMS2	Posterior emissions of EMS2	\
	CEP3	Posterior emissions of EMS3	Same as CEP	\

## 4 Results

4.1 Inverted Emissions

Figure 2 shows the spatial distribution of temporally averaged prior and posterior emissions, along with their differences, in NMVOC emissions. Hotspots of prior NMVOC emissions were prevalent across much of central and southern China. However, posterior NMVOC emissions were predominantly concentrated in the NCP, Yangtze River Delta (YRD), PRD, and Sichuan Basin (SCB), characterized by high levels of anthropogenic activity. High emissions are also located in parts of central and southern China with warm climate favorable for emitting biogenic NMVOCs. Employing TROPOMI HCHO observations as constraints led to widespread decreases of approximately 60–70% over these areas, indicating a large substantial of biogenic NMVOC emissions. In northwestern China, there was a moderate increase in NMVOC emissions. Validation efforts against 28 NDACC FTIR stations reported that TROPOMI generally displays a negative bias of -30% for HCHO concentrations exceeding 8×10^{15} molec cm^{-2}, while a positive bias of 34% is observed at clean sites with HCHO concentrations below 2.5×10^{15} molec cm^{-2} (Lambert et al., 2023). Comparisons with MAX-DOAS measurements yielded similar biases. A potential significant bias in polluted regions could exacerbate the emission reduction. Nevertheless, the large magnitude of emission reductions of 50.2% in our inversion is comparable to studies in southern China (Bauwens et al., 2016; Zhou et al., 2023), southeastern US (Kaiser et al., 2018), Africa (Marais et al., 2014), India (Chaliyakunnel et al., 2019), Amazonia (Bauwens et al., 2016), and parts of Europe (Curci et al., 2010), but opposite to the large-scale emission increase over China in Cao et al. (2018). For NO$_x$ (Figure S1), the nationwide total emissions decreased by 10.2%, with the main reductions concentrated in the NCP, YRD, parts of Central China, and most key urban areas.
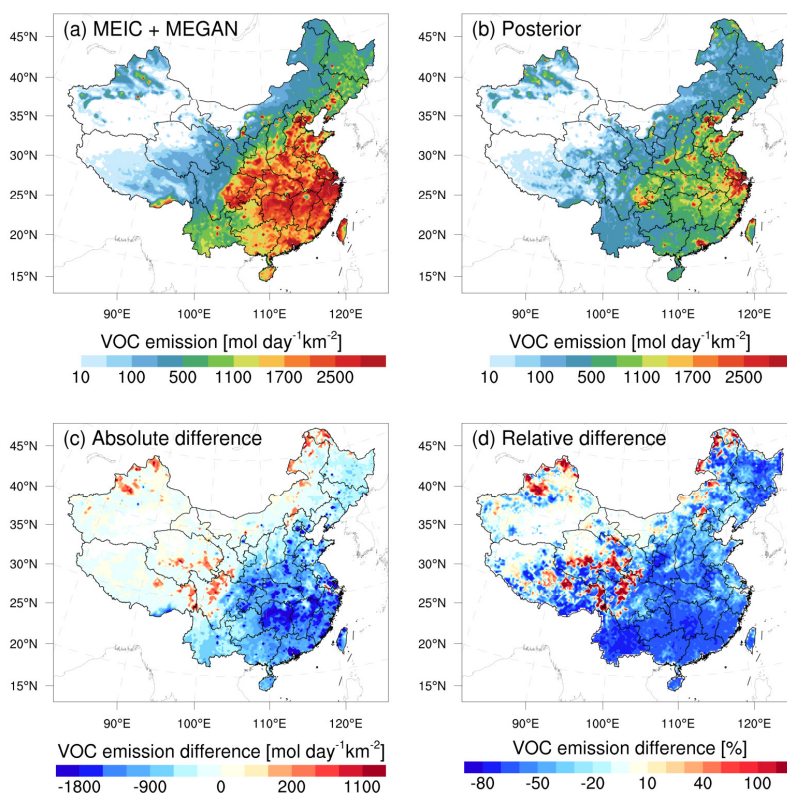
Figure 2. Spatial distribution of the time-averaged (a) prior emissions (MEIC 2020 + EMGAN), (b) posterior emissions, (c) absolute difference (posterior minus prior), and (d) relative difference of NMVOCs over China.

Table 2 shows the changes in emissions of biogenic NMVOCs across different land cover types (Figure S2) after inversion. The most significant reduction in biogenic emissions occurred within woody savannas, accounting for 26.9% of the overall reduction, followed by savannas and croplands, accounting for 21.2% and 17.2% respectively. Among all vegetation types, the broadleaf evergreen forests, recognized as the primary source of isoprene emission (Wang et al., 2021a), presented the greatest uncertainty, with NMVOC emissions experiencing a significant reduction of 66.2%. Standard emission rates in MEGAN are derived from leaf- or canopy-scale flux measurements and extrapolated globally across regions sharing similar landcover characteristics, based on very limited observations (Guenther et al., 1995). This methodology introduces biases due to the large variability in emission rates among plant species. Furthermore, DiMaria et al. (2023) optimized the temperature response

365 within MEGAN with ground-based constraints, increasing the model's temperature

366 sensitivity by a factor of five over the Amazonian. Opacka et al. (2022) optimized the

367 empirical parameter in the MEGANv2.1 soil moisture stress algorithm, resulting in

368 significant reductions in isoprene emissions and providing better agreement between

369 modelled and observed HCHO temporal variability in the central U.S. These findings

370 demonstrate that uncertainties in MEGAN parameterization also have significant

371 implications for NMVOC emission modeling.

372 **Table 2**. Prior and posterior biogenic NMVOC emissions, as well as their differences

373 for different land cover types.

Land cover type	Prior	Posterior	Difference
	Mmol/month	Mmol/month	Mmol/month (%)
Evergreen needleleaf forests	955.7	549.3	-406.4 (-42.5)
Evergreen broadleaf forests	13985.1	4728.2	-9256.8 (-66.2)
Deciduous needleleaf forests	46.6	48.8	2.2 (4.7)
Deciduous broadleaf forests	8335.5	3487.4	-4848.1 (-58.2)
Mixed forests	8731.0	3961.7	-4769.4 (-54.6)
Closed shrublands	9.7	3.7	-6.0 (-61.5)
Open shrublands	21.3	8.6	-12.8 (-59.8)
Woody savannas	39327.2	16925.2	-22402.0 (-57.0)
Savannas	28319.7	10629.4	-17690.3 (-62.5)
Grasslands	16912.7	14269.6	-2643.1 (-15.6)
Permanent wetlands	286.1	115.4	-170.8 (-59.7)
Croplands	25537.8	11215.5	-14322.2 (-56.1)
Cropland-natural vegetation mosaics	10894.7	4289.8	-6605.0 (-60.6)
Sparsely vegetated	1814.7	1644.0	-170.6 (-9.4)

374 **4.2 Evaluations for Posterior Emissions**

375 The NO$_x$ emissions were first evaluated by indirectly comparing the forward simulated

376 NO$_2$ concentrations with measurements. As shown in Figure S3, the CEP with prior

377 emissions exhibited positive biases in eastern China and negative biases in western

378 China. However, when posterior emissions were used in the VEP, a substantial

15

379   improvement in simulation performance was observed. Biases were limited to within

380   ±3 μg m^{-3}, and correlation coefficients exceeded 0.7 across the entire region. Figure 3

381   presents the simulated HCHO VCDs using prior and posterior NMVOCs emissions,

382   along with their associated biases. Both experiments showed high VCDs over central

383   and eastern China, especially in the YRD and SCB. However, the CEP displayed

384   substantial overestimation across most of mainland China, with the largest bias

385   reaching 12 × 10^{15} molec cm^{-2} in Central China. Conversely, the VEP demonstrated

386   notable improvements in both the magnitude and spatial distribution of simulated

387   HCHO columns after the inversion compared to TROPOMI retrievals. More than 84%

388   of the areas exhibited biases of less than 1 × 10^{15} molec cm^{-2}, and no significant spatial

389   variation was observed. Overall, the biases in simulated HCHO VCDs decreased by

390   75.7% after the inversion. These results emphasize the efficiency of our system in

391   reducing uncertainty in both NO$_x$ and NMVOC emissions.
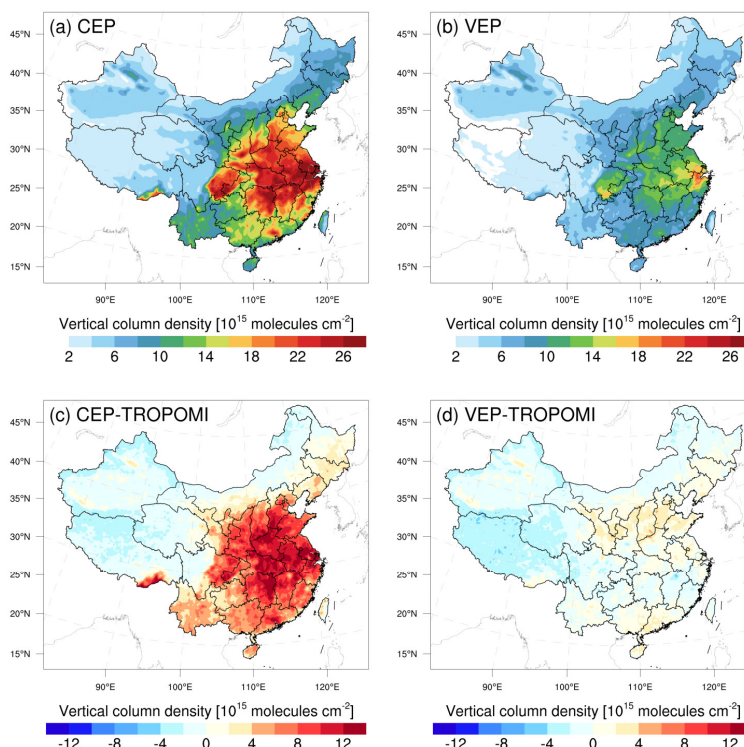
393   **Figure 3**. Simulated HCHO vertical column densities using prior (a) and posterior (b)

394   NMVOC emissions, along with their biases (c and d) against TROPOMI measurement.

395   All model results were sampled at TROPOMI overpass time.

4.3 Implications for Surface O_3

Figure 4 shows the spatial distribution of the mean bias (BIAS), root mean square error (RMSE), and correlation coefficient (CORR) for simulated O_3 concentrations in the CEP1 and VEP experiments compared to assimilated observations. Beyond the northwestern region of China, the CEP1 exhibited significant overestimation throughout the entire area, with a BIAS of 20.5 μg m^{-3}. By intercomparing 14 state-of-the-art CTMs with O_3 observations within the framework of the MICS-Asia III, Li et al. (2019) identified a substantial overestimation of annual surface O_3 in East Asia, ranging from 20 to 60 μg m^{-3}. Notably, the NCP exhibited substantial overestimations, with most models overestimating O_3 by 100–200% during May–October. In the VEP, the modeled O_3 chemical production were alleviated, especially in the southern regions of China where NMVOC emissions had significantly decreased. Overall, observation-constrained NMVOC emissions resulted in a 49.3% decrease in the BIAS, bringing it down to 10.4 μg m^{-3}. Additionally, the RMSE showed noticeable improvement due to the assimilation of HCHO observation, reducing the value from 30.9 to 23.3 μg m^{-3}. Despite a significant reduction in NMVOC emissions after inversion, notable overestimations persisted in northern provinces such as Liaoning, Hebei, Shanxi, and Shaanxi. This may be attributed to limited NMVOC constraints resulting from insufficient observations during the study period (Figures 1b and 3d). The remaining discrepancies between simulations and observations can be attributed to the combined results of intricate urban-rural sensitivity regimes and O_3 photochemistry reactions, which may not be comprehensively represented by CMAQ model, masking any potential improvement expected from the constrained emissions. The CORR was comparable between the CEP1 and VEP experiments, reflecting that the CMAQ model effectively simulated the temporal variation of O_3 concentrations. The biases at the independent sites were similar to those at the assimilated sites (Figure S4). In comparison to CEP1, the decreasing ratios in BIAS and RMSE in VEP were 46.7% and 23.4%, respectively.
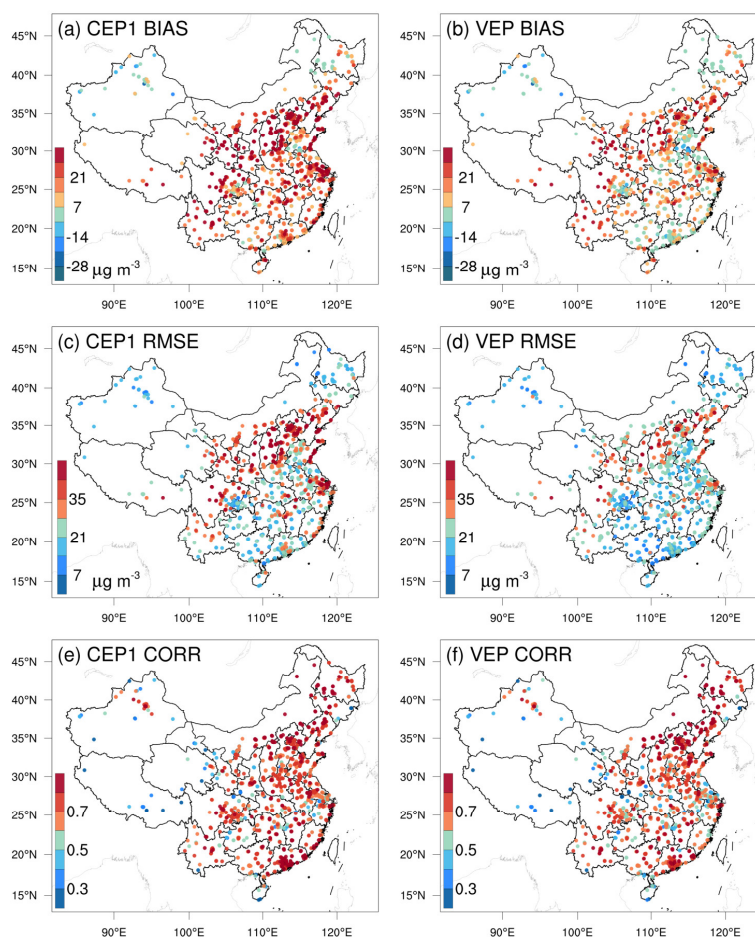
Figure 4. Spatial distribution of mean bias (BIAS, a and b), root mean square error (RMSE, c and d), and correlation coefficient (CORR, e and f) for simulated O_3 using prior (left, CEP1) and posterior (right, VEP) emissions, respectively, against assimilated observations.

Figure 5 shows the time series of simulated and observed hourly O_3 concentrations and their RMSEs, verified against surface monitoring sites. The VEP achieved better representations of diurnal O_3 variations compared with those in the CEP1, especially excelling in reproducing elevated O_3 concentrations at noon. Constraining the NMVOC emissions also led to better model simulations in terms of RMSE throughout the entire study period. Overall, the assimilation of HCHO column observations effectively reduced NMVOC emission uncertainties and consequently improved simulations of

437   HCHO and O_3. These improvements hold promise for further research into the

438   implications of emission optimizations on regional O_3 photochemistry.

439
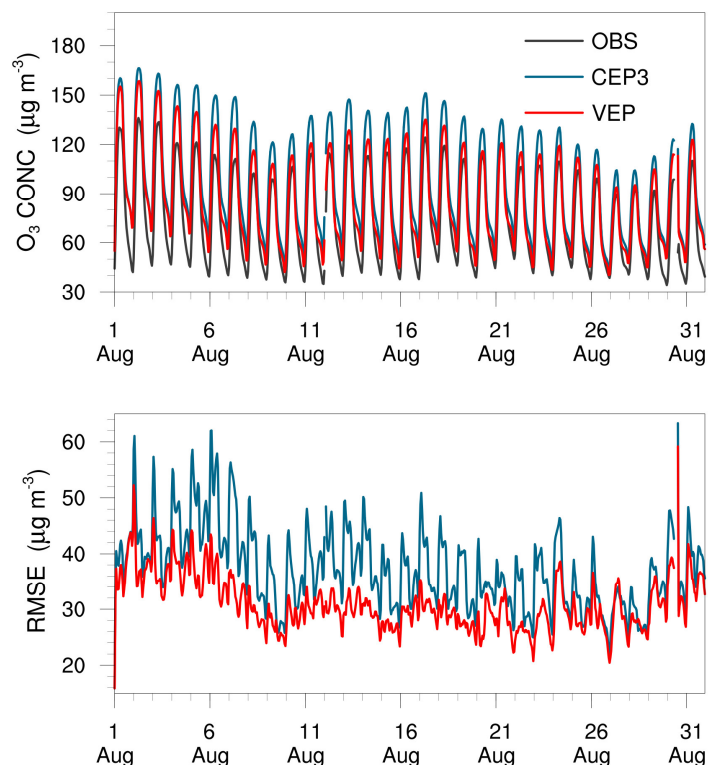
Figure 5. Time series comparison of hourly surface O_3 concentrations (μg m^{-3}) and
RMSE (μg m^{-3}) from CEP1 and VEP experiments against all observations.

442   As crucial O_3 precursors, the abundance of NMVOCs plays a significant role in

443   modulating O_3 production. Here we employed the IRRs to elucidate changes related to

444   O_3 production and loss at the surface, stemming from constrained NO_x and NMVOC

445   emissions. Figure 6 illustrates comparisons of the simulated maximum daily 8-hour

446   average (MDA8) surface O_3 levels and net reaction rates before and after the inversion.

447   The CEP1 exhibited an overestimation of O_3 levels, with a BIAS of 22.6% compared

448   to observed O_3 concentrations. This overestimation corresponded to the high net

449   chemical rates of O_3 in these areas (Figure S5). After inversion, O_3 net rates mitigated

450   in most regions. Consequently, the VEP experiment yielded results that closely aligned

451   with observations, with a BIAS of 9.2%. Referring to Figure 6e and 6f, differences in

452   production rates of O_3 closely track the changes in the NMVOC emissions (Figure 2).

The discrepancies in specific regions may be attributed to the complex nonlinear relationships associated with O_3 and its precursors, which depend on prevailing chemical regimes and regional transport. Additionally, changes in O_3 production predominantly drive the overall decrease in O_3 concentrations, outweighing changes in O_3 loss.
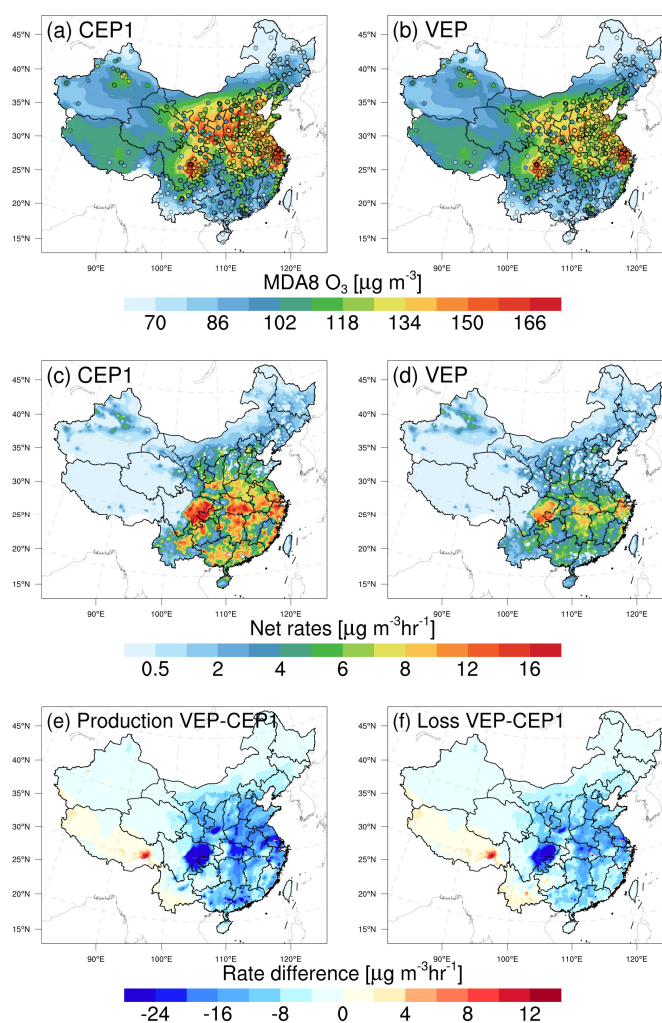

Figure 6. Comparisons of (a, b) simulated maximum daily 8-hour average (MDA8) O_3 concentrations, (c, d) net reaction rates, (e, f) and differences in production and loss rates between CEP1 and VEP experiments at the surface. Surface MDA8 O_3 values (circles) from the national control air quality stations were overlaid

463   Figure 7 shows the differences in the six principal pathways responsible for O_3 loss and

464   formation, when comparing simulations employing prior and posterior emissions. The

465   reactions of $HO_2 + NO$ and $RO_2 + NO$ are treated as the pathways leading to O_3

466   formation, whereas O_3 loss involves reactions including $NO2 + OH$, $O_3 + HO_2$, $O_3 +$

467    $NMVOCs$, and $O1D + H_2O$ (Wang et al., 2019). Our analysis was focused on the time

468   frame from 12:00 to 18:00 according to China standard time (CST). The differences

469   were computed by subtracting the simulation with posterior emissions from those with

470   prior emissions. Following the emission of NMVOCs, they undergo rapid oxidation by

471   atmospheric hydroxyl (OH) radicals. Due to the substantial decrease in NMVOC

472   emissions, there was a reduction in the production of hydroperoxy radicals (HO_2) and

473   organic peroxy radicals (RO_2) (Figure S6). Consequently, this reduction in HO_2/RO_2

474   levels, coupled with their reaction with NO, resulted in diminished O_3 production

475   (Figures 7a and 7b). A strong correlation was observed between changes in O_3

476   production via the $RO_2 + NO$ reaction and NMVOC emissions (Figure 2), consistent

477   with the findings of Souri et al. (2020). Typically, in NMVOC-rich environments, a

478   decrease in NMVOC emissions boosts OH concentrations. Consequently, we noted an

479   enhancement in the $NO_2 + OH$ reaction in the eastern and central regions of China. In

480   response to heightened HO_x concentrations over these areas, an increased O_3 loss

481   through the $O_3 + HO_x$ pathway was observed. Furthermore, we detected a substantial

482   decrease in O_3 loss through reactions with NMVOCs, especially in the southern China,

483   where substantial isoprene emissions are prevalent. This reduction was primarily

484   attributable to the decrease in NMVOC and O_3 levels. While the $NMVOC + O_3$ reaction

485   proceeds at a substantially slower rate $NMVOC + OH$, this specific chemical pathway

486   remains significant in oxidizing NMVOC and forming HO_x in forests areas (Paulson

487   and Orlando, 1996). The difference in $O1D + H_2O$ is primarily driven by the decrease

488   of O_3 photolysis. Although the rate of O_3 loss decreases in some chemical pathways,

489   overall, the rate of O_3 production dominates the changes in O_3 concentration.
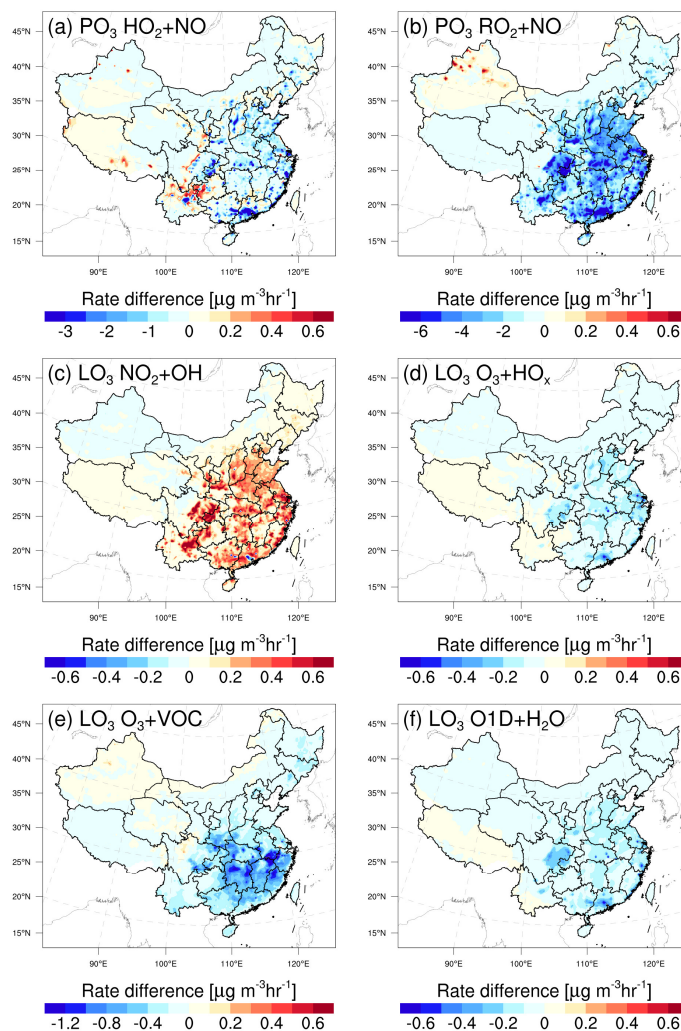
Figure 7. Differences in six major pathways of O_3 production and loss between CEP1 and VEP experiments at the surface. Time period: August 2022, 12:00–18:00 CST. PO_3 and LO_3 represent the pathways of O_3 formation and loss, respectively.

4.4 Discussions

The prior NMVOC emissions were found to be overestimated relative to the top-down constraints from TROPOMI HCHO retrievals. The results of the top-down inversion may be susceptible to uncertainties related to the inversion configuration and observational data. Particularly, background error settings affect the relative weighting of prior and observation to posterior emissions, which may potentially introduce

500 considerable uncertainty into the spatial patterns and magnitudes of the NMVOC
501 emission inversion. Another critical concern pertains to HCHO retrieval errors.
502 Correcting the low TROPOMI HCHO column biases would result in elevated posterior
503 emissions, while the opposite holds true. To investigate the impact of background error
504 on emission inversion, a sensitivity test (EMS1) was conducted, doubling the
505 background error to 80%. Compared with the base inversion, the sensitivity test
506 produced a noticeable increase in posterior NMVOC emissions in southwestern China,
507 especially in Tibet. In contrast, emissions in eastern China exhibited a slight decrease
508 (Figure S7). This can be expected, as the inversion is more inclined to deviate from the
509 a priori due to decreased confidence. However, at a national scale, the difference
510 between the two posterior emissions was nearly negligible. The substantial disparities
511 over the Tibetan Plateau between the two inversions can be attributed to the horizontal
512 HCHO inhomogeneity caused by mountain terrain and the relatively low signal-to-
513 noise ratio in the TROPOMI satellite data in the background atmosphere (Cheng et al.,
514 2023), resulting in the inclusion of more outliers in the inversion (Su et al., 2020).
515 Nevertheless, the discrepancies in NMVOC emission estimates amounted to a mere
516 0.2%, suggesting that the posterior emission estimates were not largely affected by the
517 background error setting. This can be primarily attributed to the superiority of the 'two-
518 step' inversion strategy employed within the RAPAS system.

519 Due to the spatiotemporal variability in retrieval errors, directly incorporating
520 observations into an inversion system remains a challenging task. Based on the biases
521 outlined in Vigouroux et al. (2020), another sensitivity test (EMS2) addressed the
522 existing biases in TROPOMI HCHO by reducing measurements by 25% ($<2.5\times10^{15}$
523 molec cm^{-2}) in clean regions and increasing them by 30% ($>=8\times10^{15}$ molec cm^{-2}) in
524 polluted regions. Figure 8 shows that bias-corrected HCHO columns resulted in a slight
525 decrease in NMVOC emissions in the low-pollution regions of western China, whereas
526 emissions increased in the high-pollution regions of eastern and central China,
527 particularly in the SCB and the vicinity of the YRD. In comparison to the EMDA
528 experiment, the posterior emissions from EMS1 increased by 12.8% (decreased by 43.9%
529 compared to prior emissions), indicating that the existing retrieval error in HCHO
530 measurements likely exerts an influence on the estimation of NMVOC emissions,
531 especially in heavily polluted regions. The results highlight the significance of a
532 thorough data validation for the HCHO column product. However, the emissions

533 increase in the EMS2 experiment has slightly deteriorated the performance of O_3
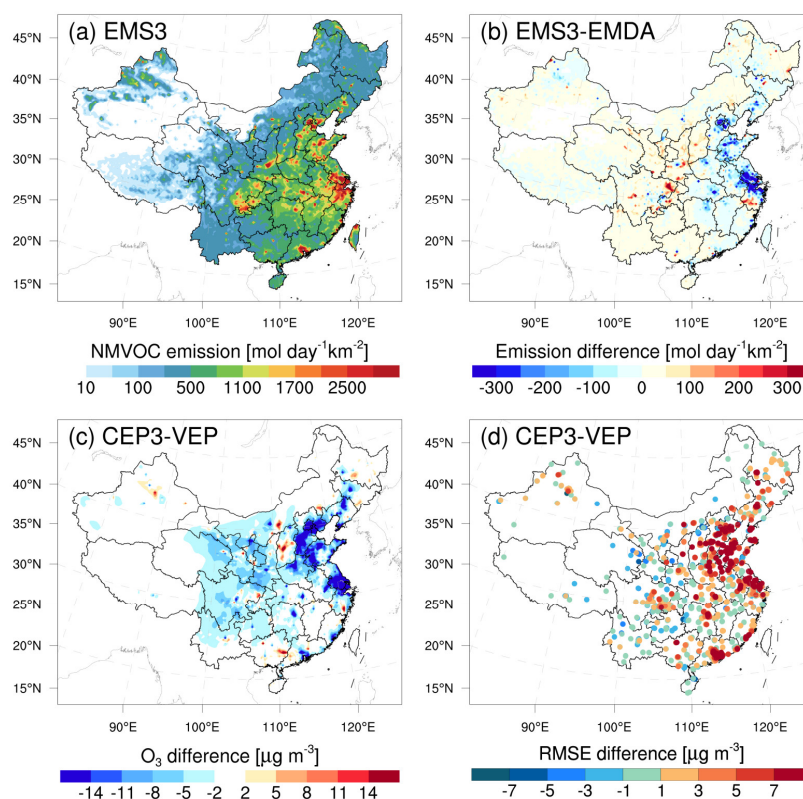
534 simulations in the CEP2.
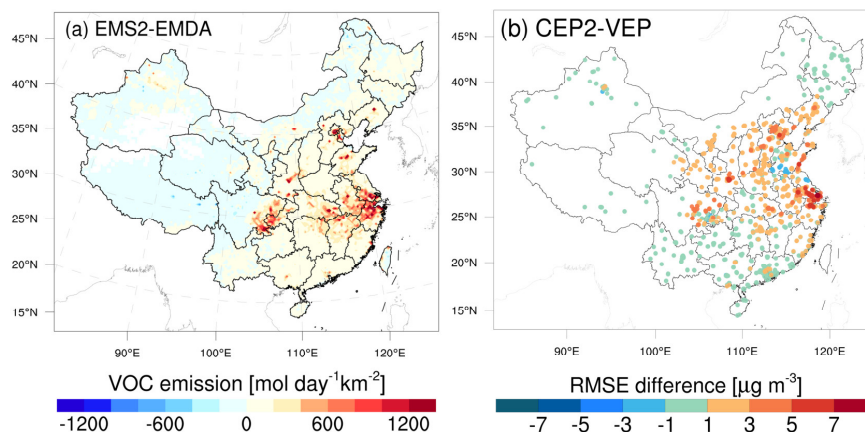
Figure 8. Spatial distribution of (a) differences in posterior emissions between EMS2

537 and EMDA, and differences in (b) RMSE between CEP2 and VEP experiments.

538 Compared with EMDA, EMS2 reduced the TROPOMI HCHO measurements by 25%

539 ($< 2.5 \times 10^{15}$ molec cm^{-2}) in clean regions and increased them by 30% ($> 8 \times 10^{15}$ molec

540 cm^{-2}) in polluted regions.

541 O_3 concentration and NO_x (VOC) emissions are positively correlated in the NO_x

542 (VOC)-limited region and negatively correlated in the VOC (NO_x)-limited region (Tang

543 et al., 2011). Therefore, the uncertainty in NO_x emissions can affect the model's

544 diagnosis of O_3-NO_x-VOC sensitivity, thereby introducing substantial model errors in

545 the HCHO yield from VOC oxidation. In the base inversion experiment (EMDA), we

546 simultaneously assimilated NO_2 and HCHO observations to optimize NO_x and

547 NMVOC emissions. To evaluate the impact of optimized NO_x emissions on O_3-VOC

548 chemistry, EMS3 disregarded the uncertainty of NO_x and focused solely on optimizing

549 NMVOC emissions. Compared to the EMDA, in areas where NO_x is significantly

550 overestimated, NMVOC emissions in the EMS3 have correspondingly decreased

551 (Figure 9b). This might be due to under high-NO_x conditions, HCHO production occurs

552 promptly, thereby compensating for the substantial amount of HCHO already present

553 in the atmosphere by reducing emissions (Chan Miller et al., 2017). Figure S8 shows

554 comparisons of concentrations and RMSE between the simulations using posterior

555 emissions from EMS3 and EMDA experiments. Compared to VEP, CEP3 showed a

larger RMSE, highlighting the necessity for simultaneous optimization of NO$_x$

emissions when evaluating the impact of NMVOC emission optimization on O$_3$.

Additionally, CEP2 using prior NO$_x$ emissions exhibited lower O$_3$ levels over parts of

NCP and YRD, as well as some urban areas (Figure 9c), but with larger biases and

RMSEs (Figure 9d). The reduction in NMVOC emissions contributed to a partial

decrease in O$_3$ concentration. More significantly, these areas typically align with VOC-

limited mechanisms (Wang et al., 2019; Wang et al., 2021b). Therefore, the

overestimation of NO$_x$ emissions (Figure S1) excessively inhibits O$_3$ accumulation due

to the titration effect, thereby disrupting the evaluation of NMVOC contributions to O$_3$.

This substantial disparity also seriously affects O$_3$ source apportionment, precursor-

sensitive area delineation, and emissions reduction policy formulation.

Figure 9. Spatial distribution of (a) posterior emissions in the EMS3 experiment, (b) differences in posterior emissions between EMS3 and EMDA, and differences in simulated (c) O$_3$ concentrations and (d) RMSE between CEP3 and VEP experiments. EMS3 did not optimize NO$_x$ emissions compared to EMDA.

25

5 Summary and Conclusions

In this study, we extended the RAPAS assimilation system with the EnKF assimilation algorithm to optimize NMVOC emissions using the TROPOMI HCHO retrievals. Taking the MEIC 2020 for anthropogenic emissions and MEGANv2.1 output for biogenic sources as a priori, NMVOC emissions over China in August 2022 were inferred. Importantly, we implicitly took the chemical feedback among VOC-NO_x-O_3 into account by simultaneously adjusting NO_x emissions using nationwide in-situ NO_2 observations. Furthermore, we quantified the impact of NMVOC emission inversion on surface O_3 pollution using the CMAQ-IRR model.

The application of TROPOMI HCHO observations as constraints led to a substantial reduction of 50.2% compared to the prior emissions for NMVOCs. A domain-wide significant decrease was found over central and southern China with abundant forests, especially for the broadleaf evergreen forests, implying a considerable overestimation of biogenic NMVOC emissions. Observation-constrained emissions significantly improved the performance of surface NO_2 and HCHO column simulations, reducing biases by 97.4% and 75.7%, respectively. This highlights the effectiveness of the RAPAS in reducing uncertainty in NO_x and NMVOC emissions. Isolating the impact of NO_x emission changes, the posterior NMVOC emissions significantly mitigated the overestimation in prior O_3 simulations, resulting in a 49.3% decrease in surface O_3 biases. This is mainly attributed to a substantial decrease in the RO2 + NO reaction rate (a major pathway for O_3 production) and an increase NO_2 + OH reaction rate (a major pathway for O_3 loss) during the afternoon, resulting in a decrease in the simulated MDA8 surface O_3 concentrations by approximately 15 μg m^{-3}.

Sensitivity inversions demonstrate the robustness of top-down emissions to variations in background error settings, yet they are sensitive to HCHO column biases, highlighting the importance of comprehensive validation studies utilizing available remote-sensing data and, if possible, airborne validation campaigns. Moreover, we found that, in comparison to optimizing NMVOC emissions alone, the joint optimization of NMVOC and NO_x emissions can significantly improve the overall performance of O_3 simulations. Ignoring errors in NO_x emissions introduces uncertainty in quantifying the impact of NMVOC emissions on surface O_3, especially in areas where overestimated NO_x emissions can unrealistically amplify titration effects,

604   highlighting the necessity of simultaneous optimization of NO_x emissions.

605

606

Data availability

608   The observations used for assimilation and the optimized emissions in this study can be

609   accessed at https://doi.org/10.5281/zenodo.10079006 (Feng and Jiang, 2023).

610

Author contribution

612   SF and FJ conceived and designed the research. SF developed the data assimilation

613   code, analyzed data, and prepared the paper with contributions from all co-authors. FJ

614   supervised and assisted in conceptualization and writing. TQ, NW, MJ, SZ, JC, FY, and

615   WJ reviewed and commented on the paper.

616

Competing interests

618   The authors declare that they have no conflict of interest.

619

Acknowledgements

628

References

630   Angot, H., McErlean, K., Hu, L., Millet, D. B., Hueber, J., Cui, K., Moss, J., Wielgasz,

631   C., Milligan, T., Ketcherside, D., Bret-Harte, M. S., and Helmig, D.: Biogenic

632   volatile organic compound ambient mixing ratios and emission rates in the

633   Alaskan Arctic tundra, Biogeosciences, 17, 6219-6236, 10.5194/bg-17-6219-2020,

634   2020.

635   Bauwens, M., Stavrakou, T., Müller, J. F., De Smedt, I., Van Roozendael, M., van der

636   Werf, G. R., Wiedinmyer, C., Kaiser, J. W., Sindelarova, K., and Guenther, A.:
637   Nine years of global hydrocarbon emissions based on source inversion of OMI
638   formaldehyde observations, Atmos. Chem. Phys., 16, 10133-10158, 10.5194/acp-
639   16-10133-2016, 2016.

640   Byun, D., and Schere, K. L.: Review of the governing equations, computational
641   algorithms, and other components of the models-3 Community Multiscale Air
642   Quality (CMAQ) modeling system, Applied Mechanics Reviews, 59, 51-77,
643   10.1115/1.2128636, 2006.

644   Cao, H., Fu, T. M., Zhang, L., Henze, D. K., Miller, C. C., Lerot, C., Abad, G. G., De
645   Smedt, I., Zhang, Q., van Roozendael, M., Hendrick, F., Chance, K., Li, J., Zheng,
646   J., and Zhao, Y.: Adjoint inversion of Chinese non-methane volatile organic
647   compound emissions using space-based observations of formaldehyde and glyoxal,
648   Atmos. Chem. Phys., 18, 15017-15046, 10.5194/acp-18-15017-2018, 2018.

649   Chaliyakunnel, S., Millet, D. B., and Chen, X.: Constraining Emissions of Volatile
650   Organic Compounds Over the Indian Subcontinent Using Space-Based
651   Formaldehyde Measurements, Journal of Geophysical Research: Atmospheres,
652   124, 10525-10545, 10.1029/2019JD031262, 2019.

653   Chan Miller, C., Jacob, D. J., Marais, E. A., Yu, K., Travis, K. R., Kim, P. S., Fisher, J.
654   A., Zhu, L., Wolfe, G. M., Hanisco, T. F., Keutsch, F. N., Kaiser, J., Min, K. E.,
655   Brown, S. S., Washenfelder, R. A., González Abad, G., and Chance, K.: Glyoxal
656   yield from isoprene oxidation and relation to formaldehyde: chemical mechanism,
657   constraints from SENEX aircraft observations, and interpretation of OMI satellite
658   data, Atmos. Chem. Phys., 17, 8725-8738, 10.5194/acp-17-8725-2017, 2017.

659   Cheng, S., Cheng, X., Ma, J., Xu, X., Zhang, W., Lv, J., Bai, G., Chen, B., Ma, S.,
660   Ziegler, S., Donner, S., and Wagner, T.: Mobile MAX-DOAS observations of
661   tropospheric NO2 and HCHO during summer over the Three Rivers' Source region
662   in China, Atmos. Chem. Phys., 23, 3655-3677, 10.5194/acp-23-3655-2023, 2023.

663   Curci, G., Palmer, P. I., Kurosu, T. P., Chance, K., and Visconti, G.: Estimating
664   European volatile organic compound emissions using satellite observations of
665   formaldehyde from the Ozone Monitoring Instrument, Atmos. Chem. Phys., 10,
666   11501-11517, 10.5194/acp-10-11501-2010, 2010.

667   De Smedt, I., Theys, N., Yu, H., Danckaert, T., Lerot, C., Compernolle, S., Van
668   Roozendael, M., Richter, A., Hilboll, A., Peters, E., Pedergnana, M., Loyola, D.,
669   Beirle, S., Wagner, T., Eskes, H., van Geffen, J., Boersma, K. F., and Veefkind, P.:
670   Algorithm theoretical baseline for formaldehyde retrievals from S5P TROPOMI
671   and from the QA4ECV project, Atmos. Meas. Tech., 11, 2395-2426, 10.5194/amt-
672   11-2395-2018, 2018.

673   DiMaria, C. A., Jones, D. B. A., Worden, H., Bloom, A. A., Bowman, K., Stavrakou, T.,
674   Miyazaki, K., Worden, J., Guenther, A., Sarkar, C., Seco, R., Park, J.-H., Tota, J.,
675   Alves, E. G., and Ferracci, V.: Optimizing the Isoprene Emission Model MEGAN
676   With Satellite and Ground-Based Observational Constraints, Journal of
677   Geophysical Research: Atmospheres, 128, e2022JD037822,
678   10.1029/2022JD037822, 2023.

679   Elbern, H., Strunk, A., Schmidt, H., and Talagrand, O.: Emission rate and chemical state
680   estimation by 4-dimensional variational inversion, Atmospheric Chemistry and
681   Physics, 7, 3749-3769, 10.5194/acp-7-3749-2007, 2007.

682   Fang, X., Shao, M., Stohl, A., Zhang, Q., Zheng, J., Guo, H., Wang, C., Wang, M., Ou,
683   J., Thompson, R. L., and Prinn, R. G.: Top-down estimates of benzene and toluene
684   emissions in the Pearl River Delta and Hong Kong, China, Atmos. Chem. Phys.,
685   16, 3369-3382, 10.5194/acp-16-3369-2016, 2016.

686   Feng, S., Jiang, F., Jiang, Z., Wang, H., Cai, Z., and Zhang, L.: Impact of 3DVAR
687   assimilation of surface PM2.5 observations on PM2.5 forecasts over China during
688   wintertime, Atmospheric Environment, 187, 34-49,
689   10.1016/j.atmosenv.2018.05.049, 2018.

690   Feng, S., Jiang, F., Wang, H., Wang, H., Ju, W., Shen, Y., Zheng, Y., Wu, Z., and Ding,
691   A.: NOx Emission Changes Over China During the COVID-19 Epidemic Inferred
692   From Surface NO2 Observations, Geophysical Research Letters, 47,
693   10.1029/2020gl090080, 2020.

694   Feng, S., Jiang, F., Wang, H., Shen, Y., Zheng, Y., Zhang, L., Lou, C., and Ju, W.:
695   Anthropogenic emissions estimated using surface observations and their impacts
696   on PM2.5 source apportionment over the Yangtze River Delta, China, Science of
697   The Total Environment, 828, 154522, 10.1016/j.scitotenv.2022.154522, 2022.

698   Feng, S., Jiang, F., Wu, Z., Wang, H., He, W., Shen, Y., Zhang, L., Zheng, Y., Lou, C.,
699   Jiang, Z., and Ju, W.: A Regional multi-Air Pollutant Assimilation System (RAPAS
700   v1.0) for emission estimates: system development and application, Geosci. Model
701   Dev., 16, 5949-5977, 10.5194/gmd-16-5949-2023, 2023.

702   Gaspari, G., and Cohn, S. E.: Construction of correlation functions in two and three
703   dimensions, Quarterly Journal of the Royal Meteorological Society, 125, 723-757,
704   10.1256/smsqj.55416, 1999.

705   Guenther, A. B., Jiang, X., Heald, C. L., Sakulyanontvittaya, T., Duhl, T., Emmons, L.
706   K., and Wang, X.: The Model of Emissions of Gases and Aerosols from Nature
707   version 2.1 (MEGAN2.1): an extended and updated framework for modeling
708   biogenic emissions, Geoscientific Model Development, 5, 1471-1492,
709   10.5194/gmd-5-1471-2012, 2012.

710   Hong, C., Zhang, Q., He, K., Guan, D., Li, M., Liu, F., and Zheng, B.: Variations of
711   China's emission estimates: response to uncertainties in energy statistics, Atmos.
712   Chem. Phys., 17, 1227-1239, 10.5194/acp-17-1227-2017, 2017.

713   Hong, Q., Liu, C., Hu, Q., Zhang, Y., Xing, C., Su, W., Ji, X., and Xiao, S.: Evaluating
714   the feasibility of formaldehyde derived from hyperspectral remote sensing as a
715   proxy for volatile organic compounds, Atmospheric Research, 264, 105777,
716   10.1016/j.atmosres.2021.105777, 2021.

717   Houtekamer, P. L., and Zhang, F.: Review of the Ensemble Kalman Filter for
718   Atmospheric Data Assimilation, Monthly Weather Review, 144, 4489-4532,
719   10.1175/mwr-d-15-0440.1, 2016.

720   Jiang, X., Guenther, A., Potosnak, M., Geron, C., Seco, R., Karl, T., Kim, S., Gu, L.,
721   and Pallardy, S.: Isoprene emission response to drought and the impact on global
722   atmospheric chemistry, Atmospheric Environment, 183, 69-83,
723   10.1016/j.atmosenv.2018.01.026, 2018.

724   Kaiser, J., Jacob, D. J., Zhu, L., Travis, K. R., Fisher, J. A., González Abad, G., Zhang,
725   L., Zhang, X., Fried, A., Crounse, J. D., St. Clair, J. M., and Wisthaler, A.: High-
726   resolution inversion of OMI formaldehyde columns to quantify isoprene emission
727   on ecosystem-relevant scales: application to the southeast US, Atmos. Chem.
728   Phys., 18, 5483-5497, 10.5194/acp-18-5483-2018, 2018.

729   Li, B., Ho, S. S. H., Li, X., Guo, L., Chen, A., Hu, L., Yang, Y., Chen, D., Lin, A., and
730   Fang, X.: A comprehensive review on anthropogenic volatile organic compounds
731   (VOCs) emission estimates in China: Comparison and outlook, Environment
732   International, 156, 106710, 10.1016/j.envint.2021.106710, 2021.

733   Li, J., Nagashima, T., Kong, L., Ge, B., Yamaji, K., Fu, J. S., Wang, X., Fan, Q., Itahashi,
734   S., Lee, H. J., Kim, C. H., Lin, C. Y., Zhang, M., Tao, Z., Kajino, M., Liao, H., Li,
735   M., Woo, J. H., Kurokawa, J., Wang, Z., Wu, Q., Akimoto, H., Carmichael, G. R.,
736   and Wang, Z.: Model evaluation and intercomparison of surface-level ozone and
737   relevant species in East Asia in the context of MICS-Asia Phase III – Part 1:
738   Overview, Atmos. Chem. Phys., 19, 12993-13015, 10.5194/acp-19-12993-2019,
739   2019.

740   Li, K., Jacob, D. J., Shen, L., Lu, X., De Smedt, I., and Liao, H.: Increases in surface
741   ozone pollution in China from 2013 to 2019: anthropogenic and meteorological
742   influences, Atmos. Chem. Phys., 20, 11423-11433, 10.5194/acp-20-11423-2020,
743   2020.

744   Li, M., Liu, H., Geng, G., Hong, C., Liu, F., Song, Y., Tong, D., Zheng, B., Cui, H.,
745   Man, H., Zhang, Q., and He, K.: Anthropogenic emission inventories in China: a
746   review, National Science Review, 4, 834-866, 10.1093/nsr/nwx150, 2017a.

747 Li, M., Zhang, Q., Kurokawa, J.-i., Woo, J.-H., He, K., Lu, Z., Ohara, T., Song, Y.,
748   Streets, D. G., Carmichael, G. R., Cheng, Y., Hong, C., Huo, H., Jiang, X., Kang,
749   S., Liu, F., Su, H., and Zheng, B.: MIX: a mosaic Asian anthropogenic emission
750   inventory under the international collaboration framework of the MICS-Asia and
751   HTAP, Atmospheric Chemistry And Physics, 17, 935-963, 10.5194/acp-17-935-
752   2017, 2017b.

753 Liu, H., Liu, Z., and Lu, F.: A Systematic Comparison of Particle Filter and EnKF in
754   Assimilating Time-Averaged Observations, Journal of Geophysical Research-
755   Atmospheres, 122, 13155-13173, 10.1002/2017jd026798, 2017.

756 Liu, Z., Wang, Y., Vrekoussis, M., Richter, A., Wittrock, F., Burrows, J. P., Shao, M.,
757   Chang, C.-C., Liu, S.-C., Wang, H., and Chen, C.: Exploring the missing source
758   of glyoxal (CHOCHO) over China, Geophysical Research Letters, 39,
759   10.1029/2012GL051645, 2012.

760 Marais, E. A., Jacob, D. J., Guenther, A., Chance, K., Kurosu, T. P., Murphy, J. G.,
761   Reeves, C. E., and Pye, H. O. T.: Improved model of isoprene emissions in Africa
762   using Ozone Monitoring Instrument (OMI) satellite observations of formaldehyde:
763   implications for oxidants and particulate matter, Atmos. Chem. Phys., 14, 7693-
764   7703, 10.5194/acp-14-7693-2014, 2014.

765 Marsh, D. R., Mills, M. J., Kinnison, D. E., Lamarque, J.-F., Calvo, N., and Polvani, L.
766   M.: Climate Change from 1850 to 2005 Simulated in CESM1(WACCM), Journal
767   of Climate, 26, 7372-7391, 10.1175/JCLI-D-12-00558.1, 2013.

768 Mo, Z., Huang, S., Yuan, B., Pei, C., Song, Q., Qi, J., Wang, M., Wang, B., Wang, C.,
769   Li, M., Zhang, Q., and Shao, M.: Deriving emission fluxes of volatile organic
770   compounds from tower observation in the Pearl River Delta, China, Science of
771   The Total Environment, 741, 139763, 10.1016/j.scitotenv.2020.139763, 2020.

772 Mu, M., Randerson, J. T., van der Werf, G. R., Giglio, L., Kasibhatla, P., Morton, D.,
773   Collatz, G. J., DeFries, R. S., Hyer, E. J., Prins, E. M., Griffith, D. W. T., Wunch,
774   D., Toon, G. C., Sherlock, V., and Wennberg, P. O.: Daily and 3-hourly variability
775   in global fire emissions and consequences for atmospheric model predictions of
776   carbon monoxide, Journal of Geophysical Research-Atmospheres, 116,
777   10.1029/2011jd016245, 2011.

778 Opacka, B., Müller, J.-F., Stavrakou, T., Miralles, D. G., Koppa, A., Pagán, B. R.,
779   Potosnak, M. J., Seco, R., De Smedt, I., and Guenther, A. B.: Impact of Drought
780   on Isoprene Fluxes Assessed Using Field Data, Satellite-Based GLEAM Soil
781   Moisture and HCHO Observations from OMI, Remote Sensing, 14, 2021, 2022.

782 Palmer, P. I., Abbot, D. S., Fu, T.-M., Jacob, D. J., Chance, K., Kurosu, T. P., Guenther,
783   A., Wiedinmyer, C., Stanton, J. C., Pilling, M. J., Pressley, S. N., Lamb, B., and

784 Sumner, A. L.: Quantifying the seasonal and interannual variability of North
785   American isoprene emissions using satellite observations of the formaldehyde
786   column, Journal of Geophysical Research: Atmospheres, 111,
787   10.1029/2005JD006689, 2006.

788 Paulson, S. E., and Orlando, J. J.: The reactions of ozone with alkenes: An important
789   source of HOx in the boundary layer, Geophysical Research Letters, 23, 3727-
790   3730, 10.1029/96GL03477, 1996.

791 Pierce, T., Geron, C., Bender, L., Dennis, R., Tonnesen, G., and Guenther, A.: Influence
792   of increased isoprene emissions on regional ozone modeling, Journal of
793   Geophysical Research: Atmospheres, 103, 25611-25629, 10.1029/98JD01804,
794   1998.

795 Ren, J., Guo, F., and Xie, S.: Diagnosing ozone–NOx–VOC sensitivity and revealing
796   causes of ozone increases in China based on 2013–2021 satellite retrievals, Atmos.
797   Chem. Phys., 22, 15035-15047, 10.5194/acp-22-15035-2022, 2022.

798 Seco, R., Holst, T., Davie-Martin, C. L., Simin, T., Guenther, A., Pirk, N., Rinne, J., and
799   Rinnan, R.: Strong isoprene emission response to temperature in tundra vegetation,
800   Proceedings of the National Academy of Sciences, 119, e2118014119,
801   doi:10.1073/pnas.2118014119, 2022.

802 Skamarock, W. C., and Klemp, J. B.: A time-split nonhydrostatic atmospheric model
803   for weather research and forecasting applications, Journal Of Computational
804   Physics, 227, 3465-3485, 10.1016/j.jcp.2007.01.037, 2008.

805 Souri, A. H., Nowlan, C. R., González Abad, G., Zhu, L., Blake, D. R., Fried, A.,
806   Weinheimer, A. J., Wisthaler, A., Woo, J. H., Zhang, Q., Chan Miller, C. E., Liu,
807   X., and Chance, K.: An inversion of NOx and non-methane volatile organic
808   compound (NMVOC) emissions using satellite observations during the KORUS-
809   AQ campaign and implications for surface ozone over East Asia, Atmos. Chem.
810   Phys., 20, 9837-9854, 10.5194/acp-20-9837-2020, 2020.

811 Souri, A. H., Chance, K., Bak, J., Nowlan, C. R., González Abad, G., Jung, Y., Wong,
812   D. C., Mao, J., and Liu, X.: Unraveling pathways of elevated ozone induced by
813   the 2020 lockdown in Europe by an observationally constrained regional model
814   using TROPOMI, Atmos. Chem. Phys., 21, 18227-18245, 10.5194/acp-21-18227-
815   2021, 2021.

816 Su, W., Liu, C., Chan, K. L., Hu, Q., Liu, H., Ji, X., Zhu, Y., Liu, T., Zhang, C., Chen,
817   Y., and Liu, J.: An improved TROPOMI tropospheric HCHO retrieval over China,
818   Atmos. Meas. Tech., 13, 6271-6292, 10.5194/amt-13-6271-2020, 2020.

819 Tang, X., Zhu, J., Wang, Z. F., and Gbaguidi, A.: Improvement of ozone forecast over
820   Beijing based on ensemble Kalman filter with simultaneous adjustment of initial

821   conditions and emissions, Atmospheric Chemistry And Physics, 11, 12901-12916,
822   10.5194/acp-11-12901-2011, 2011.

823 van der Werf, G. R., Randerson, J. T., Giglio, L., van Leeuwen, T. T., Chen, Y., Rogers,
824   B. M., Mu, M., van Marle, M. J. E., Morton, D. C., Collatz, G. J., Yokelson, R. J.,
825   and Kasibhatla, P. S.: Global fire emissions estimates during 1997-2016, Earth
826   System Science Data, 9, 697-720, 10.5194/essd-9-697-2017, 2017.

827 Vigouroux, C., Langerock, B., Bauer Aquino, C. A., Blumenstock, T., Cheng, Z., De
828   Mazière, M., De Smedt, I., Grutter, M., Hannigan, J. W., Jones, N., Kivi, R.,
829   Loyola, D., Lutsch, E., Mahieu, E., Makarova, M., Metzger, J. M., Morino, I.,
830   Murata, I., Nagahama, T., Notholt, J., Ortega, I., Palm, M., Pinardi, G., Röhling,
831   A., Smale, D., Stremme, W., Strong, K., Sussmann, R., Té, Y., van Roozendael,
832   M., Wang, P., and Winkler, H.: TROPOMI–Sentinel-5 Precursor formaldehyde
833   validation using an extensive network of ground-based Fourier-transform infrared
834   stations, Atmos. Meas. Tech., 13, 3751-3767, 10.5194/amt-13-3751-2020, 2020.

835 Wang, H., Yan, R., Xu, T., Wang, Y., Wang, Q., Zhang, T., An, J., Huang, C., Gao, Y.,
836   Gao, Y., Li, X., Yu, C., Jing, S., Qiao, L., Lou, S., Tao, S., and Li, Y.: Observation
837   Constrained Aromatic Emissions in Shanghai, China, Journal of Geophysical
838   Research: Atmospheres, 125, e2019JD031815, 10.1029/2019JD031815, 2020.

839 Wang, H., Wu, Q., Guenther, A. B., Yang, X., Wang, L., Xiao, T., Li, J., Feng, J., Xu,
840   Q., and Cheng, H.: A long-term estimation of biogenic volatile organic compound
841   (BVOC) emission in China from 2001–2016: the roles of land cover change and
842   climate variability, Atmos. Chem. Phys., 21, 4825-4848, 10.5194/acp-21-4825-
843   2021, 2021a.

844 Wang, N., Lyu, X., Deng, X., Huang, X., Jiang, F., and Ding, A.: Aggravating O3
845   pollution due to NOx emission control in eastern China, Science of The Total
846   Environment, 677, 732-744, 10.1016/j.scitotenv.2019.04.388, 2019.

847 Wang, W., van der A, R., Ding, J., van Weele, M., and Cheng, T.: Spatial and temporal
848   changes of the ozone sensitivity in China based on satellite and ground-based
849   observations, Atmos. Chem. Phys., 21, 7253-7269, 10.5194/acp-21-7253-2021,
850   2021b.

851 Warneke, C., de Gouw, J. A., Del Negro, L., Brioude, J., McKeen, S., Stark, H., Kuster,
852   W. C., Goldan, P. D., Trainer, M., Fehsenfeld, F. C., Wiedinmyer, C., Guenther, A.
853   B., Hansel, A., Wisthaler, A., Atlas, E., Holloway, J. S., Ryerson, T. B., Peischl, J.,
854   Huey, L. G., and Hanks, A. T. C.: Biogenic emission measurement and inventories
855   determination of biogenic emissions in the eastern United States and Texas and
856   comparison with biogenic emission inventories, Journal of Geophysical Research:
857   Atmospheres, 115, 10.1029/2009JD012445, 2010.

858   Whitaker, J. S., and Hamill, T. M.: Ensemble data assimilation without perturbed
859   observations, Monthly Weather Review, 130, 1913-1924, 10.1175/1520-
860   0493(2002)130<1913:Edawpo>2.0.Co;2, 2002.

861   Wolfe, G. M., Kaiser, J., Hanisco, T. F., Keutsch, F. N., de Gouw, J. A., Gilman, J. B.,
862   Graus, M., Hatch, C. D., Holloway, J., Horowitz, L. W., Lee, B. H., Lerner, B. M.,
863   Lopez-Hilifiker, F., Mao, J., Marvin, M. R., Peischl, J., Pollack, I. B., Roberts, J.
864   M., Ryerson, T. B., Thornton, J. A., Veres, P. R., and Warneke, C.: Formaldehyde
865   production from isoprene oxidation across NOx regimes, Atmos. Chem. Phys., 16,
866   2597-2610, 10.5194/acp-16-2597-2016, 2016.

867   Yuan, B., Kaser, L., Karl, T., Graus, M., Peischl, J., Campos, T. L., Shertz, S., Apel, E.
868   C., Hornbrook, R. S., Hills, A., Gilman, J. B., Lerner, B. M., Warneke, C., Flocke,
869   F. M., Ryerson, T. B., Guenther, A. B., and de Gouw, J. A.: Airborne flux
870   measurements of methane and volatile organic compounds over the Haynesville
871   and Marcellus shale gas production regions, Journal of Geophysical Research:
872   Atmospheres, 120, 6271-6289, 10.1002/2015JD023242, 2015.

873   Zhang, Q., Streets, D. G., Carmichael, G. R., He, K. B., Huo, H., Kannari, A., Klimont,
874   Z., Park, I. S., Reddy, S., Fu, J. S., Chen, D., Duan, L., Lei, Y., Wang, L. T., and
875   Yao, Z. L.: Asian emissions in 2006 for the NASA INTEX-B mission, Atmos.
876   Chem. Phys., 9, 5131-5153, 10.5194/acp-9-5131-2009, 2009.

877   Zheng, B., Tong, D., Li, M., Liu, F., Hong, C., Geng, G., Li, H., Li, X., Peng, L., Qi, J.,
878   Yan, L., Zhang, Y., Zhao, H., Zheng, Y., He, K., and Zhang, Q.: Trends in China's
879   anthropogenic emissions since 2010 as the consequence of clean air actions,
880   Atmospheric Chemistry And Physics, 18, 14095-14111, 10.5194/acp-18-14095-
881   2018, 2018.

882   Zhou, B., Guo, H., Zeren, Y., Wang, Y., Lyu, X., Wang, B., and Wang, H.: An
883   Observational Constraint of VOC Emissions for Air Quality Modeling Study in
884   the Pearl River Delta Region, Journal of Geophysical Research: Atmospheres, 128,
885   e2022JD038122, 10.1029/2022JD038122, 2023.

886